Video Article

Conducting Elevated Temperature Normal and Combined Pressure-Shear Plate Impact Experiments Via a Breech-end Sabot Heater System

Bryan Zuanetti[1], Tiaxue Wang[1], Vikas Prakash[1]

[1]Department of Mechanical and Aerospace Engineering, Case Western Reserve University

Correspondence to: Vikas Prakash at vikas.prakash@case.edu

URL: https://www.jove.com/video/57232
DOI: doi:10.3791/57232

Keywords: Engineering, Issue 138, Elevated temperature plate impact experiments, normal plate impact, combined pressure-shear plate impact, near-melt temperatures, ultra-high strain rates, dynamic material behavior under extreme conditions

Date Published: 8/7/2018

Citation: Zuanetti, B., Wang, T., Prakash, V. Conducting Elevated Temperature Normal and Combined Pressure-Shear Plate Impact Experiments Via a Breech-end Sabot Heater System. *J. Vis. Exp.* (138), e57232, doi:10.3791/57232 (2018).

Abstract

A novel approach for conducting normal and/or combined pressure-shear plate impact experiments at test temperatures up to 1000 °C is presented. The method enables elevated temperature plate-impact experiments aimed towards probing dynamic behavior of materials under thermomechanical extremes, while mitigating several special experimental challenges faced while performing similar experiments using the conventional plate impact approach. Custom adaptations are made to the breech-end of a single-stage gas-gun at Case Western Reserve University; these adaptations include a precision-machined extension piece made from SAE 4340 steel, which is strategically designed to mate the existing gun-barrel while providing a high tolerance match to the bore and keyway. The extension piece contains a vertical cylindrical heater-well, which houses a heater assembly. A resistive coil heater-head, capable of reaching temperatures of up 1200 °C, is attached to a vertical stem with axial/rotational degrees of freedoms; this enables thin metal specimens held at the front-end of a heat-resistant sabot to be heated uniformly across the diameter to the desired test temperatures. By heating the flyer plate (in this case, the sample) at the breech-end of the gun-barrel instead of at the target-end, several critical experimental challenges can be averted. These include: 1) severe changes in the alignment of the target plate during heating due to the thermal expansion of the several constituents of the target holder assembly; 2) challenges that arise due to the diagnostics elements, (*i.e.*, polymer holographic gratings, and optical probes) being too close to the heated target assembly; 3) challenges that arise for target plates with an optical window, where crucial tolerances between the sample, bond layer, and window become increasingly difficult to maintain at high temperatures; 4) in the case of combined compression-shear plate impact experiments, the need for high-temperature resistant diffraction gratings for the measurement of transverse particle velocity at the free surface of the target; and 5) limitations imposed on the impact velocity necessary for unambiguous interpretation of the measured free surface velocity versus time profile due to thermal softening and possibly yielding of the bounding target plates.By utilizing the adaptations mentioned above, we present results from a series of reverse geometry normal plate impact experiments on commercial purity aluminum at a range of sample temperatures. These experiments show decreasing particle velocities in the impacted state, which are indicative of material softening (decrease in post-yield flow stress) with increasing sample temperatures.

Video Link

The video component of this article can be found at https://www.jove.com/video/57232/

Introduction

In engineering applications, materials are subjected to a wide range of conditions, which can be static or dynamic in nature, coupled with high levels of deformation and temperatures ranging from room to near the melting point. Under these thermomechanical extremes the material behavior can vary drastically; thus, over nearly a century, several experiments have been developed aimed towards probing the dynamic response and/or other characteristics of material behavior while under controlled loading regimes[1,2,3,4,5,6,7,8,9,10,11,12,13,14]. For metals loaded at low to intermediate strain rates (10^{-6}-10^{0} /s), servo-hydraulic or precision screw universal testing machines have been used to study the material response subjected to various loading modes and levels of deformation. But as the applied strain rates increase beyond the intermediate strain rates (*i.e.*, >10^{2}/s), other experimental techniques become necessary in order to probe the mechanical response. For example, at loading rates of 10^{3}/s up to 5 × 10^{4}/s full-sized or miniaturized Split-Hopkinson pressure bars enable such measurements to be made[8,15].

Traditionally, light gas-guns and/or explosively driven plate impact experiments have been utilized to study the dynamic inelasticity and other phenomenon such as spallation, or phase transformation that occur with very high strain rates (10^{5}-10^{7}/s)[16,17,18,19,20,21,22], or combinations of high pressures and dynamic loading. Customarily, plate impact experiments involve the launch of a flyer plate carried by a sabot initially at the breech-end of the gas-gun, which then travels down the length of the gun-barrel and is made to collide with a carefully aligned stationary target plate at the impact chamber. As a result of the impact, normal and/or combined pressure and shear stresses are generated at the flyer/target interface, which travel through the spatial dimensions of the plates as longitudinal and/or combined longitudinal and transverse stress waves. The arrival of these waves at the rear surface of the target plate affect the instantaneous free surface particle velocity of the target plate, which is monitored typically via interferometric techniques. In order to allow the interpretation of the measured particle velocity versus time history, it is

necessary that plane-waves with a front parallel to the impact surface be generated upon impact[14,23]. To ensure the former, impact must occur with an impact tilt angle on the order of less than one milli-radian[12,24], with impact surfaces of flatness better than a couple micrometers[5,25].

Plate impact experiments have been adapted to include heating elements which enable investigations of material behavior to extend into thermomechanical extremes[26,27,28,29]. These adaptations usually involve the addition of an induction coil, or of a resistive heater element to the target-end of the gas-gun; though these adaptations have been shown to be experimentally feasible, the approach inherently leads to special experimental challenges which require careful considerations. Some of these experimental complications include differential thermal expansion of the various constituents of the target holder assembly and/or alignment fixture while heating the target (sample) plate, which requires in-real-time alignment adjustments, usually made with remotely controlled alignment tools with continuous feedback in order to maintain crucial parallelism tolerance between the sample and target plate. In the case of the pressure-shear plate impact experimental scheme, heating the sample requires conventional polymer gratings be replaced by high-temperature resistant metallic gratings in order to monitor transverse particle velocity at the free surface of the target plate. Moreover, heating of the sample can add limitations on the impact velocity that can be employed in certain experimental schemes, such as in the high strain rate combined pressure-and-shear plate impact configuration, where special considerations may be required to prevent unambiguous interpretation of the experimental results, which are calculated using the acoustic impedance of the front and rear target plates which may be temperature dependent. Lastly, for other experimental schemes, which require a target plate with an optical window, tolerances between the sample, bond layer, and/or coatings become increasingly difficult to maintain at high temperatures[19].

To alleviate the experimental challenges mentioned above, we have made custom adaptations to the existing single-stage gas-gun located at Case Western Reserve University (CWRU)[7,30,31,32]. These modifications enable thin metal specimens held at the front-end of a heat-resistant sabot to be heated to temperatures in excess of 1000 °C, prior to firing, which allow high temperature normal and/or combined pressure-shear plate impact experiments to be conducted. In contrast to most of the conventional approaches employed for elevated temperature plate impact studies, this method has been shown to alleviate several of the experimental challenges described above. For example, this approach has been utilized to feasibly achieve tilt angles of less than one milli-radian without the need for remote tilt adjustment[30], or additional optical elements for monitoring tilt changes during the experiment. Second, since the target plate remains under ambient temperatures, this method does not require the need for special high-temperature resistant holographic gratings for the measurement of transverse particle velocity in oblique impact experiments; additionally, higher impact velocities can be utilized without the risk of yielding the target plate, and thus, reduce the complexity in the interpretation of the experimental results. To add, this approach can be utilized to perform high temperature reverse-geometry normal plate impact experiments which provide Us-Up relationships for a choice sample material. These can be obtained via impedance matching techniques, or additionally, an analysis of the rarefaction fan from the back surface of the sample which carry information regarding changes in sample shock velocity during unloading[33,34]. In the elevated temperature combined pressure-shear plate impact configuration, this approach enables the dynamic inelasticity of thin films to be studied up to a wide temperature and plastic deformation range, and strain-rates up to 10^7/s depending of the thickness of the thin specimen[16,27,29].

We will present the protocols necessary for performing a typical elevated temperature plate impact experiment discussed above. This will be followed by a section dedicated to representative results obtained using the present technique. Lastly, a discussion of the results will be presented prior to a conclusion.

Protocol

1. Sample and Target Material Preparation

NOTE: In the following protocol, we will detail the steps necessary for preparing the sample and target materials, which will be later used in a reverse geometry normal plate impact experiment. In this setup, a flyer plate (also the sample), held at the front of a sabot, will be launched via a single stage gas gun and made to impact a stationary target plate housed in the target chamber of the gas gun. A typical flyer and target plate assembly described in the following protocol is shown schematically in **Figure 1**.

1. Section a 99.999% commercial purity polycrystalline aluminum rod into disks which will later be used as the flyer plates (samples).
   NOTE: This can be done by using a slow speed saw in order to prevent high temperatures and residual stresses in the work piece.
2. Face and turn the sample disks on a lathe to a diameter of 76 mm and thickness of 5.6 mm.
3. Drill three equispaced holes 5 mm in diameter on a 62 mm diameter bold circle on the sample disks, which will later be used to secure the samples to the sabot.
4. Grind both sides of the sample plates in order to achieve a flatness and parallelism tolerance of nearly 10 μm over the diameter of the samples.
   1. Perform a rough lap on the sample plate surfaces using a commercial lapping machine with relatively coarse particle size (10 - 20 μm).
      NOTE: A weight can be added in this step until the lapped surfaces reach an even dull grey, indicating uniformity across the diameter of the disk.
   2. Carefully clean the lapped samples using ethanol to remove any residual particles, and mineral oil. Then, polish both surfaces of the sample plates using 1 μm diamond paste on a polishing cloth.
   3. Check the flatness of the samples by observing light bands through an optical flat in contact with the surface of interest under a green monochromatic light source[16].
      NOTE: Flatness can be quantified by observing the curvature of the light bands on the surface of the sample, or by counting the number of bands across the diameter as shown in **Figure 2**.
      1. Move-on to the next step if 3 light bands or less are seen across the sample diameter indicating that a flatness of approximately 2 μm. Otherwise, repeat steps 1.4.1 - 1.4.3 until 3 light bands or better is achieved.

5. Repeat steps 1.1 - 1.3 to fabricate the target plates. Section a precipitation hardened (high strength) alloy rod (**Table of Materials**) into disks and then machine these to a diameter of 25 mm and thickness of 7 mm. Finally, grind both sides flat to approximately 10 μm.

1. Lap both surfaces of the target plates on a lapping machine using 15 µm alumina powder in mineral oil until the surfaces achieve an even dull grey appearance.
   NOTE: An equivalent particle size of diamond slurry can be used to achieve faster removal rates, and better surface reflectively. Additionally, weights can be used.
2. Repeat step 1.4.2.
3. Check the flatness of the target plates by repeating step 1.4.3. If 1 light band or better is observed proceed to the next step. Otherwise, repeat steps 1.4.1 - 1.4.3 until 1 light band or better is achieved. If holographic gratings are necessary, proceed to step 1.5.4, otherwise skip to step 1.6.

6. Utilize a similar procedure as described in step 1.1 - 1.3 to fabricate the aluminum ring.
   1. Section an aluminum tube with the outer and inner diameters of 41 mm and 32 mm, respectively, into rings and then face the sides to a thickness of 7 mm.
   2. Drill six 3 mm diameter slots equispaced on a 34.5 mm diameter bolt circle. These will later house six voltage biased copper pins, which will enable tilt measurements to be made at impact.
   3. Grind, lap, clean, and polish both surfaces of the aluminum rings by using the procedures detailed in step 1.4.

7. Adhere the flat target plate to the aluminum ring using a two-parts epoxy mixture on a flat securing rig as shown in **Figure 3**. Allow the epoxy to cure overnight at room temperature.
   NOTE: The two parts are secured to a flat steel stage using three screws which are gently hand tightened so that the applied pressures on the target and the ring prevent the epoxy from leaking outwards.
   1. Remove any left-over adhesive from the radial slots or from the surface of the plates using acetone.
   2. Insert the target plate/aluminum ring assembly into the POM ring.
      NOTE: The POM disk will later be mounted on-to a target holder with rotational degrees of freedom, which will allow the alignment of the test materials within the gun-barrel.
   3. Mark the position of the six radial slots on the inner step of the POM ring and drill six thru-thickness holes at the marked locations.
   4. Section 6 copper pins from a spool of 15 AWG enameled copper wire with the length of ~ 50 mm and remove the enameled insulation layer from two of them. Press the pins into the slots in a symmetric pattern: two ground pins are placed in opposite locations of the circle. Push the pins through the slots and leave approximately 2 mm protruding outwards from the surface of the ring.
      NOTE: The pins are used for measuring the tilt angle and provide the trigger signal.
   5. Adhere bent-ends of the copper pins to the rear-surface of the POM ring using extra fast-setting epoxy.
   6. Use a low viscosity two parts epoxy mixture to seal the gap between the aluminum ring and the inner wall of the POM ring. Allow the epoxy to cure overnight at room temperature.

8. Remove the excess 2 mm of copper pins protruding from the surface of the aluminum ring. First section the excess pins with a rotary tool, and then sand the remaining down to the surface using wet 300 grit sand paper, until pins are nearly flush to the surface of the aluminum ring.
   1. Lap, clean and polish the entire assembly by repeating steps 1.4.1-1.4.3. Ensure that the entire lapped assembly is flat to within 2 - 3 light bands.
   2. Solder the ends of the six copper pins at the back-surface of the POM ring, and mount the POM ring to the target holder using four 6.35 mm diameter POM pins.

2. Assembly of Custom Heat-Resistant Sabot

1. Gather the assembly components for the heat resistant sabot, shown in **Figure 4**.
2. Attach an eyebolt at the bottom-end of the aluminum cap, and secure a sealing O-ring and a PTFE key in the grooves of the cap.
   NOTE: The key and O-ring are used to prevent the tilt and rotation of the sabot during its travel down the gun-barrel.
   1. Pull the thermo-couple wire through the hole on the bottom of the cap, and secure the thermo-couple wire into a connector.
3. Adhere the cap to the back-end, and the fully-fired alumina silicate Lava rock tube to the front-end of the aluminum tube using two-parts quick setting epoxy.
4. Pull the thermo-couple probe through the hole in the 76.2 mm diameter H13 tool-steel alloy sample holder.
5. Adhere the H13 sample holder to the front-end of the Lava tube using high temperature cement, or equivalent high temperature adhesive.
6. Apply the high temperature cement around the 25 mm diameter and 3 mm thick Lava disk sitting on top of the inner thru-thickness 19 mm diameter concentric hole of the H13 holder. Allow the high temperature cement to dry overnight at room temperature.
7. Secure the sample to H13 sample holder using three alumina screws, and ensure that the flatness of the sample does not change by using the protocol described in 1.4.3.

3. Assembly of the Test Materials within the Gas-Gun

1. Clean the front surface of the sample and target with isopropyl alcohol, and then use tape to secure first surface mirrors to the surface of each.
2. Screw tighten a 3-axis motion stage onto an extruding rod above the gun barrel within the impact chamber, and attach the prism holder carrying a precision optical prism onto the stage.
3. Pull a rope through the gun barrel, and attach the rope to the sabot via the eyebolt on the aluminum cap.
4. Place the sabot into gun barrel with the sample facing towards the impact chamber, and place the target holder assembly into the target chamber facing the sample.
5. Align the position of the target by adjusting the four POM positioning pins until the first-surface mirror on the target is aligned to the first-surface mirror on the sample.

1. Perform a rough align of the parallelism between the sample and target plates using a diffused bulb and a reflective mirror. Adjust the stage until a single continuous reflected image of the bulb can be seen from all of the surfaces on the alignment prism.

6. Use an auto-collimator[24] to achieve the fine alignment.
    1. Adjust the stage until the reflected image of the cross from the back surface of the prism is aligned with the image reflected from the first-surface mirror on the sample.
    2. Adjust the target assembly by turning the positioning screws on the target holder until the reflected image of the cross from the back surface of the prism is aligned with the image reflected from the first-surface mirror on the target.

7. Remove the first-surface mirrors from the sample and target. Also remove the reflective mirror, prism, prism holder and the adjustment stage from the impact chamber.
8. Pull the sabot to the breech-end of gas-gun using the rope, and then remove the rope from the cap.
9. Leave ~ 2.5 mm distance between the sabot and the heater head and accordingly adjust the length of the screws which prevent the back motion of the sabot towards the breech.
10. Connect the thermal-couple to the temperature diagnostic monitor.
    NOTE: The thermal-couple wire on the temperature monitor end has been put inside the barrel through the vacuum pipe using a feedthrough.

4. Arrangement and Alignment of the Laser-Based Diagnostics

1. Put two threaded anchors in the holes on the back of the focuser probe holder. Tighten two screws through the anchors until they reach the POM to enable the freedom to change the incident beam angle.
    1. Drill a thru-thickness hole on the bottom of the focuser probe holder, and secure it on a threaded cylindrical magnet.
    2. Pull an optical fiber focuser probe through an aluminum tube, and glue the probe to the aluminum tube by applying extra fast-set epoxy around the probe head and the tip of the aluminum tube. Push the probe head as forward into the tube as possible, but make sure to leave the probe lens away from epoxy. Wait until the extra fast-set epoxy is hardened.
    3. Connect the optical focuser to the all-fiber-optics NDI/TDI interferometer[31], and place the focuser assembly on the target holder aiming towards the rear-surface of the target.

2. Turn on the laser, in this case a 2W Erbium fiber coupled laser, to 0.2-0.4 W power. Next, adjust the position of the focuser probe using the screws attached on the focuser assembly until proper light coupling is achieved and the acquired signal is optimized.
3. Adjust the variable ratio coupler to match the intensity of the reference and Doppler-shifted light until the signal shown in the oscilloscope is optimized.
    NOTE: If transverse motion diagnostics are needed, please refer to steps 4.5 - 4.6.
4. Put two threaded anchors in the holes on the back of the POM focuser holder, and then tighten the two screws through the anchors until they touch the POM.
    1. Drill a thru-thickness hole on the bottom of the focuser probe holder, and secure it on a threaded cylindrical magnet.
    2. Pull an optical fiber collimator probe through an aluminum tube, and glue the probe to the aluminum tube by applying extra fast-set epoxy around the probe head and the tip of the aluminum tube. Push the probe head as forward into the tube as possible, but make sure to leave the probe lens away from epoxy. Wait until the extra fast-set epoxy is hardened.
    3. Repeat the above steps in 4.4 to make two assemblies and put them in the impact chamber.

5. Adjust the positions and the angles of the receiving optical fiber collimators with the magnet and the two screws on the POM holder until the intensity of the first-order diffracted beams measured by the power monitors is optimized.
6. Disconnect the power monitor and connect the two receiving collimators to the all-fiber-optics TDI interferometer[31].

5. Execution of High Temperature Reverse Geometry Normal/Pressure-Shear Plate Impact Experiments

1. Secure the primary flange by tightening the four clamps on the entrance of the impact chamber, and then close the chamber using a polyester film bolted to a secondary flange.
2. Increase the seal pressure to ~207 kPa, and then close the gas-gun at the breech-end by tightening the screws in the flange.
3. Turn on the breech-end vacuum pump, and then turn on the target chamber-end vacuum pump.
4. Ensure that there is no motion of the sabot towards the chamber caused by the pressure difference between the front and the back of the sabot. Wait until the chamber is evacuated to a pressure less than 100 mTorr.
5. Turn on the laser-amplitude-based sabot impact velocity measurement system.
6. Move the heater down to the marked position and turn on the heater. Increase the temperature of the heater with 100 °C increments until the desired sample temperature is reached.
7. Pressurize the firing dump chamber to ~1103 kPa, and the load chamber to a desired level depending on the chosen impact velocity. Also, secure the sabot catcher to the impact chamber.
8. Turn off the heater and immediately move the heater up upwards towards the heater-well. Record the temperature displayed on the temperature diagnostic monitor measured by the sabot thermocouple at the sample surface.
9. Immediately open the seal valve and release the firing dump chamber once the seal pressure drops to zero.

Representative Results

An 82.5 mm bore, 6 m length, single-stage gas gun at CWRU capable of accelerating 0.8 kg projectiles to speeds up to 700 m/s was used in conducting the present experiments. **Figure 5** shows a photograph of the modified gas-gun facility at CWRU. Prior to firing, the custom designed sabot is housed within the heater extension piece, shown in **Figure 6**. The extension piece carries a vertical heater-well enabling a resistive coil heater to move in and out of the path of the sabot. This heater coil enables the flyer plate held at the front of the sabot to be heated via free radiation under vacuum to the desired test temperatures. The sabot is custom designed to carry the heated flyer plate while mitigating heat flow from the flyer plate into the sabot body, thus mitigating the risk for seizure of the sabot due to the possible thermal expansion of the sabot body. The custom sabot design is shown schematically in **Figure 7**. The key to the design is the ceramic insulator tube, made from fully fired alumina silicate, chosen for its low thermal conductivity, low thermal expansion, and excellent resilience as compared to other commercially available machinable ceramics. Once the desired test-temperature is attained, the heater head is manually moved out of the path of the projectile and housed within the heater-well. Just prior to firing the gas gun, the temperature of the sample is recorded via a thermocouple probe attached to the front of the flyer plate. For this particular experiment, the velocity of the projectile is approximately 100 m/s, moreover, assuming constant acceleration, it takes just over one tenth of a second for the projectile to reach the target, thus, the temperature recorded just prior to firing is believed to be a good estimate for the initial sample temperature at impact. Next, the firing protocol is performed. When the seal pressure in the breech reaches the atmospheric pressure, and the firing pressure is dumped into the firing dump chamber, the piston maintaining a seal between the load chamber and gun barrel is displaced backwards. This allows for high pressure gas to rapidly flow outwards from the breech and launch the sabot. The sabot travels down the length of the gun-barrel and is made to impact with the stationary target plate at the impact chamber.

The custom designed sabot enables the flyer plate to be either normal or inclined in respect to the axis of motion. **Figure 8** and **Figure 9** schematically show the reverse normal, and oblique plate impact configurations, respectively; however, only the reverse normal plate impact configuration is described in the present manuscript. **Figure 10** shows a photograph of a typical target holder assembly used in these experiments. The rotational degrees of freedom enable precise alignment of the target plate to the flyer plate. Alignment is performed using a precision machined prism in conjunction with an autocollimator, as shown schematically in **Figure 11**. During the alignment, parallel beams from the autocollimator reflect off the surface of the prism, target, and flyer plate; a third beam reflects off the interior surface of the prism. The reflected beams remain parallel if and only if the flyer and target plate surfaces are parallel to each other, and perpendicular to the rear surface of the prism. The in-coming parallel beams will then converge to form a single image on the reticle of the autocollimator signifying that the surfaces are aligned.

For the reverse normal plate impact scheme, upon impact, normal stresses are generated at the flyer/target interface which travel through the spatial dimensions of the plates as a longitudinal stress wave with a front parallel to the impact surface (provided that the flatness, and parallelism tolerances have been met). Upon impact, the voltage-biased pins come into contact with the metallic flyer plate carried by the sabot, creating a path to ground. The signals from the shorted pins are monitored through the tilt acquisition circuit, digitized, and then recorded through an oscilloscope.These signals provide quantitative information regarding the maximum tilt at impact, as well as, the tilt plane, and additionally provide a trigger pulse for the oscilloscope to begin recording signals from the normal motion diagnostics. In the present study, an in-house-built all fiber optics based combined normal and transverse displacement interferometer is used to monitor the free surface motion of the target (**Figure 12**). **Figure 13** shows the raw data recorded during a successful reverse geometry normal plate impact experiment. The data in this plot enable the user to confirm that the protocol stated above has been performed correctly. Shown in red is the signal provided by the tilt acquisition circuit. For this experiment, the difference in time between the shorting of the first and last voltage biased pins is approximately 180 ns, which indicates that the distance between the first, and last point of contact during impact was about 18 μm (given that the projectile traveled at 100 m/s), so the maximum tilt at impact measured across the 34.5 mm bolt circle was approximately 0.52 mrad. If the alignment protocol is not performed satisfactorily, a much larger tilt time would be observed, and a tilt level greater than a couple mrad could convolute the shock wave profile measured at the free surface. Another indication of a successful experiment is the difference in time between the first shorted pin and the arrival of the longitudinal wave at the free surface of the target plate. The stress wave generated at impact travels at a constant speed provided that the target plate remains elastic. For the alloy rod used in this study, the speed of the longitudinal wave is approximately 5820 m/s, thus knowing the thickness of the target, 7 mm, suggests that the longitudinal wave should arrive approximately 1.2 μs after impact. In **Figure 13**, the arrival of the longitudinal stress wave is marked by a rapid beat frequency and amplitude variation of the signal acquired from the normal motion diagnostics. A delayed arrival of the longitudinal stress wave might indicate a large tilt, inelasticity of the target plate, or improper target assembly preparation.

Figure 14 shows the schematic of the stress versus particle velocity diagram for a general normal shock compression plate-impact experiment in which both the pre-heated flyer and the target plate can undergo elastic-plastic deformation at impact. The loci of all stress/particle velocity states for the target plate under uniaxial strain is represented by the black curve passing through the origin, while the loci of all stress/particle velocity states for the flyer is represented by the black curve intersecting the particle velocity axis at the projectile velocity. The red curve intersecting the particle velocity axis at the projectile velocity is meant to illustrate the possible effect of temperature on the locus of states for the sample. For an impact against a room temperature sample, at the sample/target interface the target plate moves from an un-loaded state (1), to a loaded state (3), following the dash-dot line (Raleigh line) with a slope equal to the longitudinal impedance of the target plate material at state (3), while the sample plate moves from an unloaded state (2) to a loaded state (3), following the Raleigh line with a slope equal to the longitudinal impedance of the sample at state (3). The intersection between these two lines reveal the maximum stress and velocity states achievable through impedance matching during this experiment at the sample/target interface. Moreover, the stress/particle velocity states at the sample/target interface affect the particle velocity states at the free surface of the target plate, this shown as state (4). Impact against a sample with a lower longitudinal acoustic impedance, would result in a change in achievable states at the sample/target interface from (3) to (5), and consequently, at the free surface of the target from (4) to (6), thus, this shows how slight changes in the longitudinal acoustic impedance of the sample are detectable by monitoring the particle velocity at the free surface of the target plate.

Note, that particle velocity at the free surface of target is at least twice that of the particle velocity at the sample/target interface, but this factor changes as a function of the speed of plastic wave propagation, consequently, the stress state at the sample/target interface is estimated using[7]

$$\sigma_T(t'^n) = \sigma_F(t'^n) = \rho_T C_{LT} \frac{1}{1 + \frac{C_{LT}}{C^n}} V_{fs}(t^n) \qquad (1)$$

where t^n is a discritzed time interval represented as $t^n = nh$, where h is the inverse of the sampling rate of the oscilloscope (2.5 x 10^{10} / s), $t'^n = t^n - L/C^n$ where L is the thickness of the target plate and C^n is an average stress dependent speed of plastic propagation in the target plate measured at the free surface at time t^n. ρ_T, and C_{LT} are the density and elastic longitudinal wave speed of the target plate respectively, and V_{fs} is the measured particle velocity at the free surface of the target plate. Additionally, from the measured free surface particle velocity corresponding to the velocity plateau (state (3)), the longitudinal acoustic impedance of the flyer (sample) can be estimated using[32]

$$\rho_F C_F^{(3)} = \frac{\rho_T C_T^{(3)} V_{fs}^{(3)}}{\left(1 + \frac{C_T^{(3)}}{C_{LT}}\right) V_o - V_{fs}^{(3)}} \qquad (2)$$

Figure 15 shows the free-surface particle velocity trace obtained from the normal motion diagnostics. This trace initially manifests a relatively sharp rise in velocity related to the dynamics of the impact, followed by a plateau resulting from an impedance match between the flyer and target plates which is sustained through the duration of the experiment. The initial velocity rise relates directly to the dynamic strength, and incipient plastic flow of the target plate material, whereas, the velocity at the shock plateau is related to the impedance match between the target and flyer plates. The figure clearly shows progressively decreasing particle velocities at the wave-front and particle velocity plateau as a function of increasing temperature, suggesting possible thermal softening and/or monotonically decreasing longitudinal impedance of the sample material with temperature.

A more interesting result can be seen in **Figure 16**, which shows the normal free surface particle velocity trace obtained from reverse geometry normal plate impact experiments performed on commercial purity polycrystalline magnesium. Similarly, to **Figure 15**, **Figure 16**(a) shows monotonically decreasing particle velocities at the shock plateau with increasing temperatures in the range of 23 – 610 ˚C, however, at temperatures beyond this level (*i.e.*, 617, 630 ˚C), a reversal of this trend can be clearly observed. This increase in particle velocity suggests an increase in the shock impedance of the sample material, moreover, assuming that the elastic constants of the material decrease as a function of increasing temperature, then an increase in the shock impedance, in this case, suggests an increase in the yield strength and/or plastic modulus of the sample material. Carefully looking at **Figure 16**(b) it can be seen that the increase in particle velocity at the shock plateau is accompanied by an increase in the particle velocity levels throughout the initial rise in the particle velocity trace, which correlates with the stress levels at the sample/target interface during the incipient plasticity of the sample material. **Figure 17** shows micrographs of cross-sections of the impact surface of post-test specimens. The images show two noticeable effects on the microstructure as a result of increasing temperature. First, the images show grain ripening with increasing sample temperature, which is expected. However, the images also show a change in twin band formations, which manifest as tabular features or lines with a finite width that cut through grains. Carefully looking at the images corresponding to temperatures ranging from 23 – 500 ˚C, a clear reduction in twin bands are observed with increasing temperature. However, at higher temperatures (*i.e.*, 610, 617, 630 ˚C) a re-emergence of these twin bands are observed, which suggests that twin band formation is favored at the latter-end of this temperature range. Since plastic deformation in magnesium is accommodated through competing mechanisms of twin band formations and slip, it is plausible that the favored twin band formation observed at the highest test temperature case suggests that slip has become more difficult under these conditions.

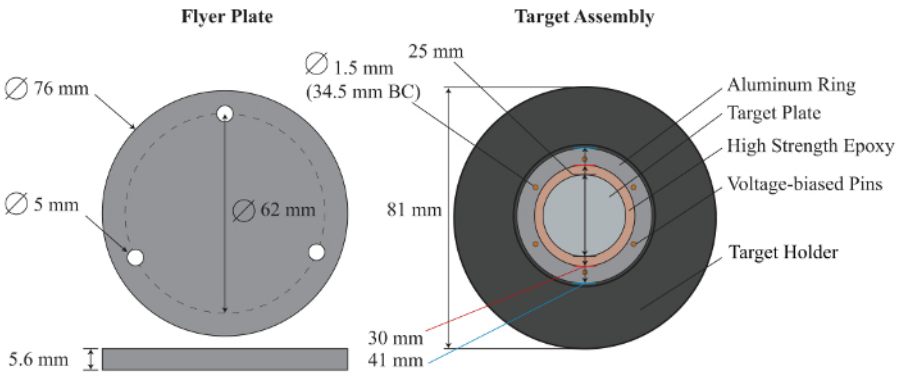

Figure 1: Schematic of a typical flyer plate and target plate assembly. This figure shows a simple schematic of the flyer and target plate assemblies used in a present experimental configuration. An in-depth protocol for preparing these parts are detailed in steps 1.1-1.7. Please click here to view a larger version of this figure.

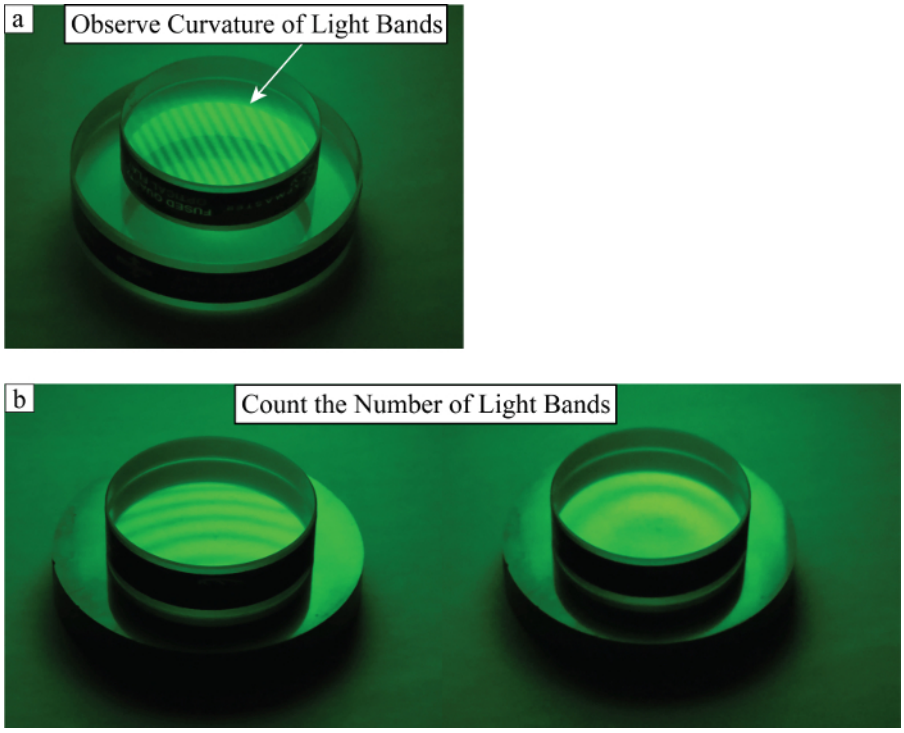

Figure 2: Photograph of the flatness measurement method. This figure shows the flatness measurement on the plates by placing an optical flat on the surface of interest under a green monochromatic light. Flatness can be quantified (**a**) by observing the curvature of the light bands on the surface of the sample, or (**b**) by counting the number of bands across the diameter. Please click here to view a larger version of this figure.

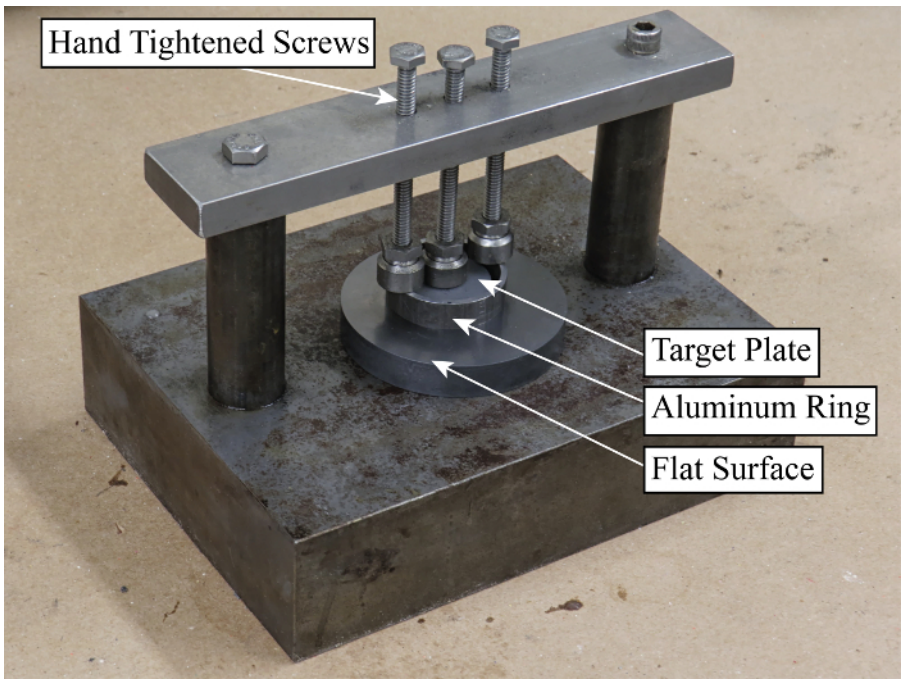

Figure 3: Photograph of a flat securing rig. This figure shows the target plate and the aluminum ring are secured to a flat steel stage using three screws which are gently hand tightened so that the applied pressures on the target and the ring prevent the epoxy from leaking out. Please click here to view a larger version of this figure.

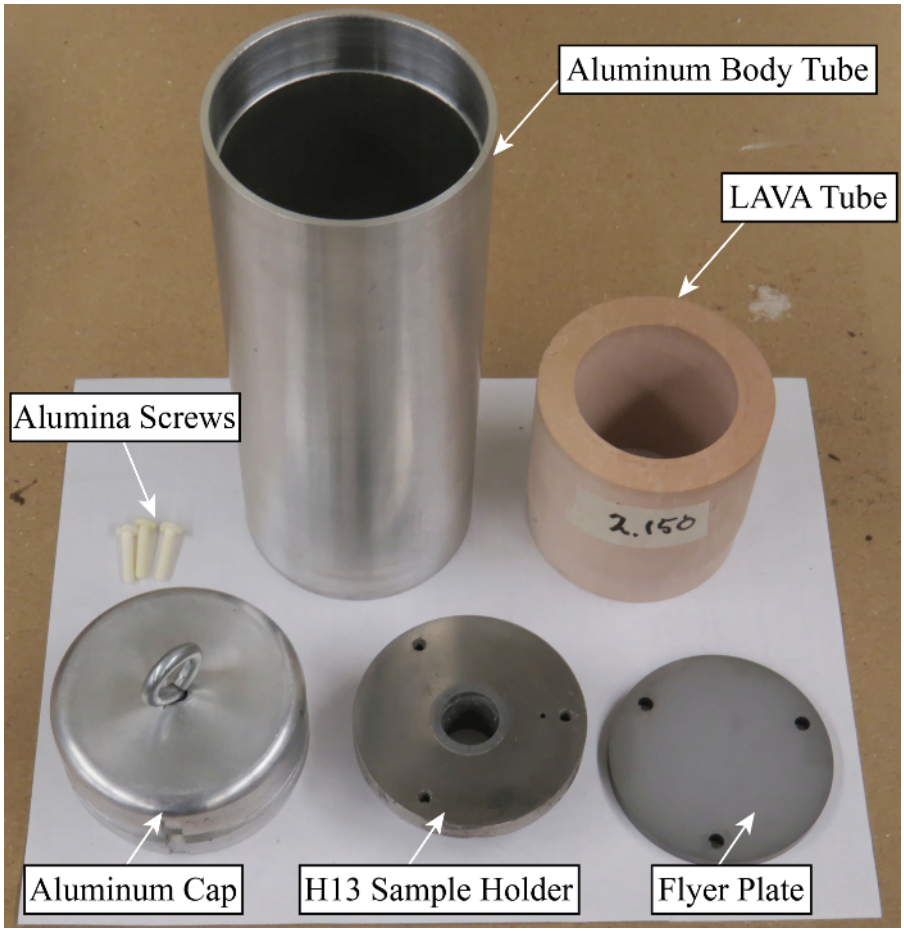

Figure 4: Photograph of the components in the sabot design. This figure shows the components of the assembly of custom heat-resistant sabot. Please click here to view a larger version of this figure.

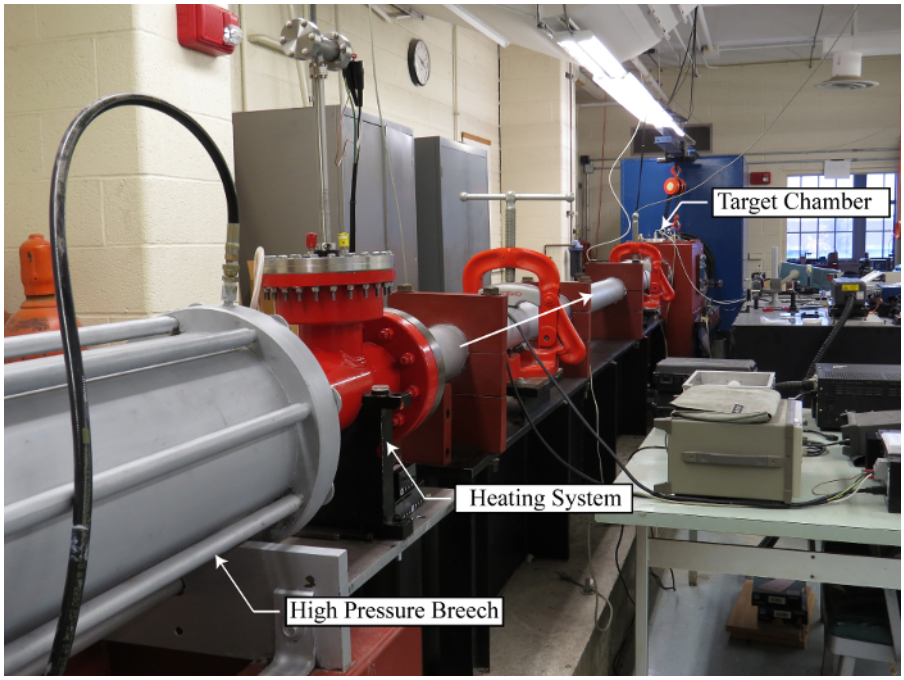

Figure 5: Gas-gun facility at CWRU. This figure shows a photograph of the single stage gas-gun facility at Case Western Reserve University. Shown in red is the custom designed heating system which mates with the existing gun-barrel, and enables desired temperature conditions to be imparted to the sabot. Please click here to view a larger version of this figure.

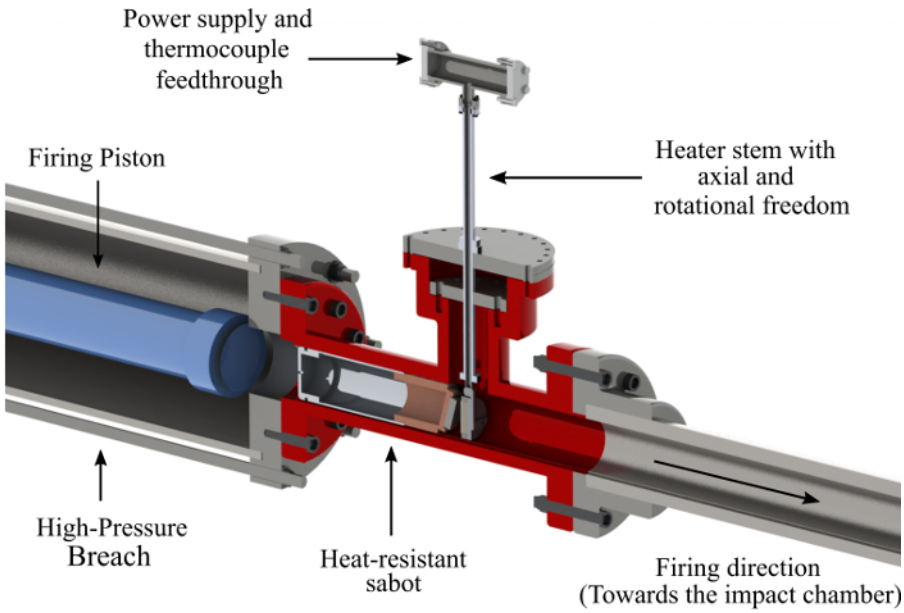

Figure 6: Schematic of the heating system. This figure shows a schematic of the heating system attached to the high pressure single stage gas-gun breech. The custom extension piece incorporates a heater-well which houses a resistive heater coil held on a stem with axial and rotational degrees of freedom. This coil can move in-line with the projectile and heat thin metal specimens held at the front of the sabot to temperatures in excess of 1000 °C, prior to firing. Please click here to view a larger version of this figure.

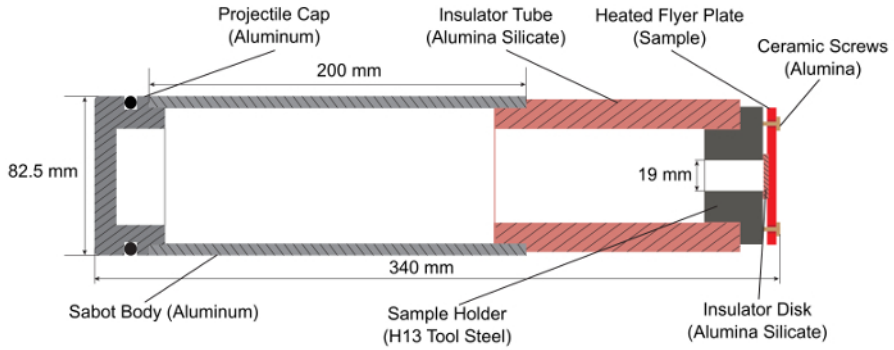

Figure 7: Schematic of the heat-resistant sabot. This figure shows a schematic of the sabot used in current experimental configuration. The alumina silicate tube helps mitigate heat flow from the heated thin metal specimen to the sabot body, thus minimizing the risk of seizure of the sabot within the gun-barrel due to possible thermal expansion of the sabot body. Please click here to view a larger version of this figure.

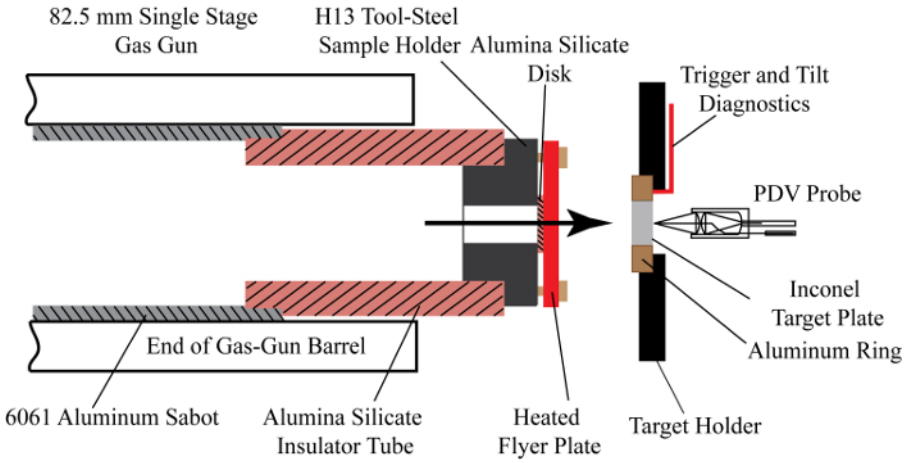

Figure 8: Schematic of the high temperature reverse configuration normal plate impact experiment. The sabot carrying the heated flyer plate is propelled down the gun barrel and made to collide with the target assembly. Upon impact, pins lapped flush with the target plate provide trigger pulse and tilt diagnostics, while the free surface motion of the target plate is monitored via custom built PDV. Please click here to view a larger version of this figure.

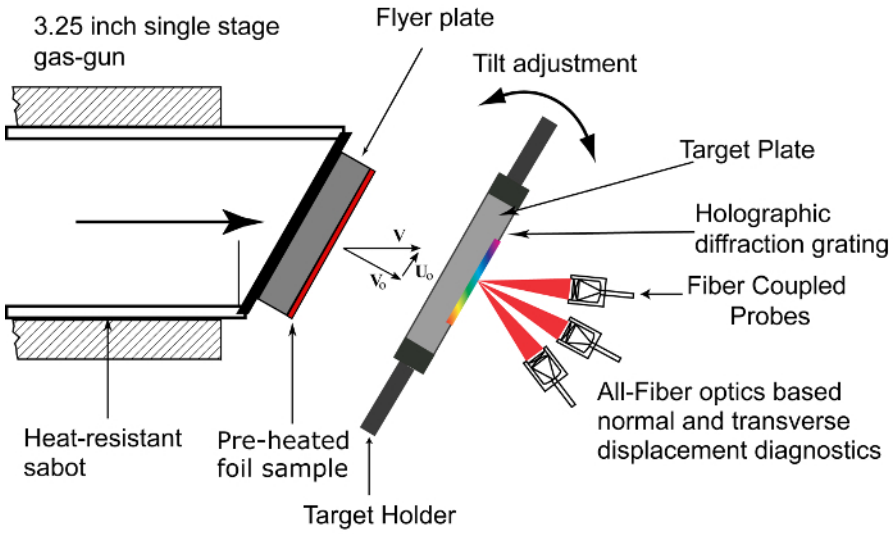

Figure 9: Schematic of the typical symmetric oblique plate impact experiment. In this configuration, a flyer plate is inclined in respect to the axis of motion, which upon impact provides both normal and transverse components of motion in respect to the normal of the impact surface. Please click here to view a larger version of this figure.

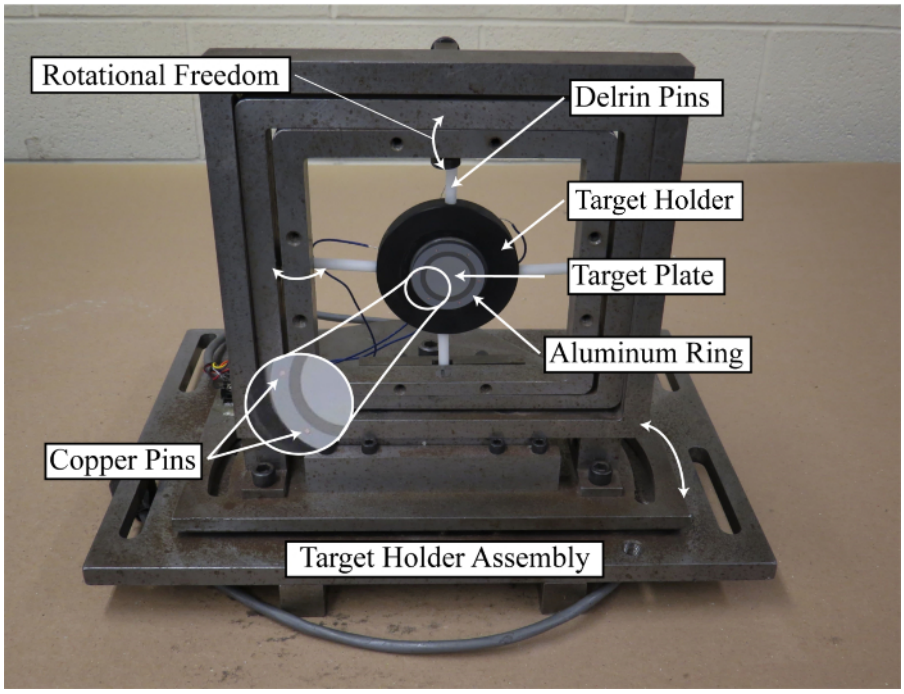

Figure 10: Photograph of a typical target holder assembly. This figure shows the typical target holder assembly used for either normal or oblique plate impact experiments. The target assembly shown in the center is attached to the target holder via POM pins, and rotational degrees of freedom enable precise alignment to be made. Please click here to view a larger version of this figure.

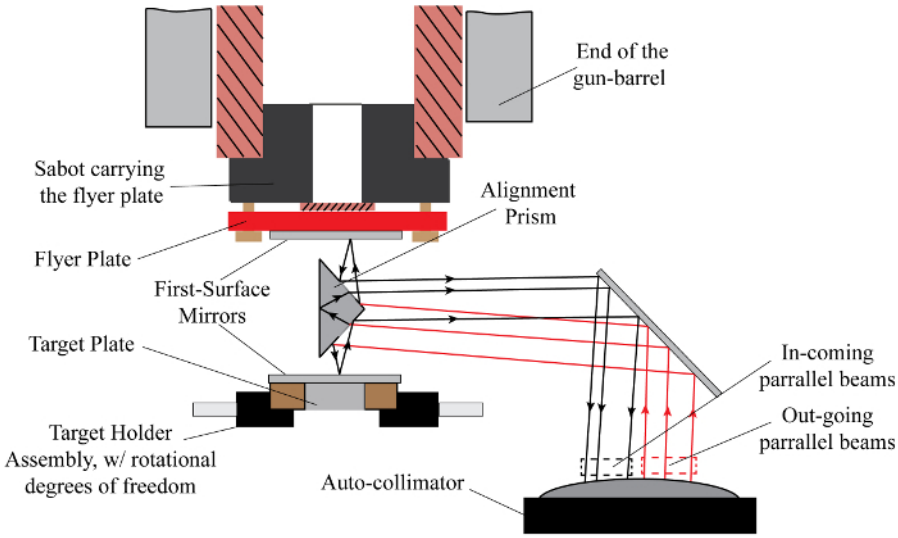

Figure 11: Prism Alignment Scheme. This figure shows an illustration of the alignment scheme for the flyer and target plates using a high precision right angle prism in conjunction with an autocollimator. Parallel beams (shown in red) from the autocollimator reflect off the surface of the prism, target, and flyer plate, a third beam reflects of the interior surface of the prism. The reflected beams (shown in black) maintain parallelism given that the flyer and target plate surfaces are parallel to each other, and perpendicular to the rear surface of the prism. The in-coming parallel beams converge to form a single image on the reticle of the autocollimator. Please click here to view a larger version of this figure.

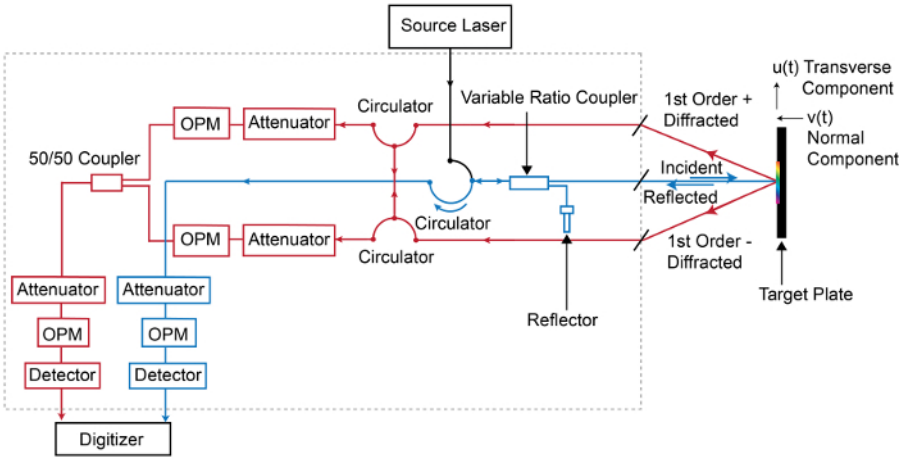

Figure 12: Schematic of the custom all fiber-optics based combined normal and transverse displacement interferometer system. This configuration uses a modified PDV, shown in blue, to both monitor the normal motion of the target plate, and illuminate a holographic grating at the free surface of the target, creating multiple order diffracted beams. These beams (usually first order) can be coupled back into the fibers and combined to create beat frequency variations proportional to the transverse motion of the target plate, this is shown in red. Please click here to view a larger version of this figure.

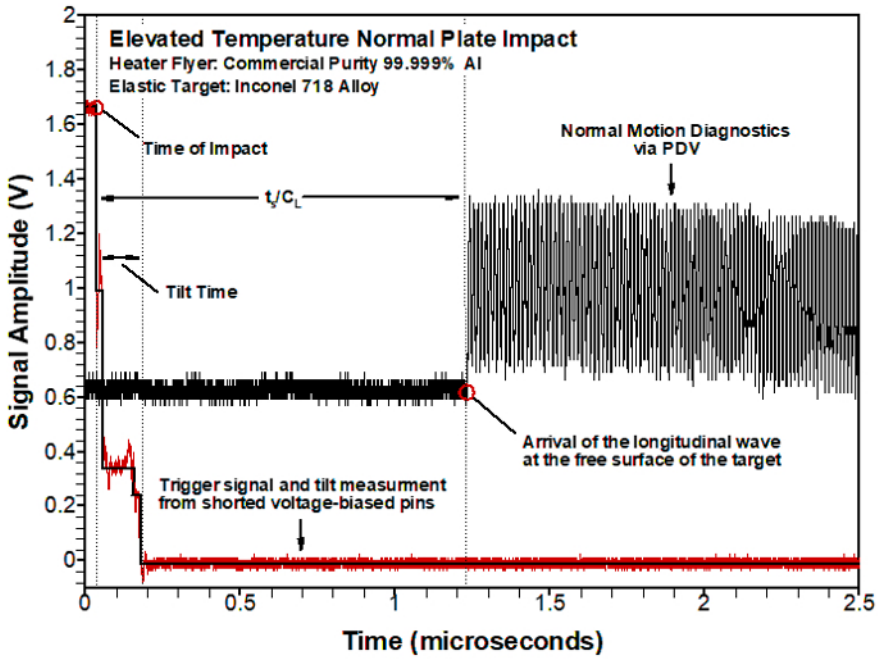

Figure 13: Raw data from a typical normal plate impact experiment. This figure shows the recorded signal obtained during a typical reverse geometry normal plate impact experiment. Shown in red is the signal obtained from the shorted voltage-biased pins attached to the aluminum ring during impact. The difference in time between the first and last shorted pin give an estimate of the maximum tilt at impact, and the order of which the pins are shorted enable estimates regarding the tilt plane to be made. Shown in black is the signal obtained from our normal motion diagnostics, here the beat frequency variations are related to the normal motion of the free surface of the target plate. Please click here to view a larger version of this figure.

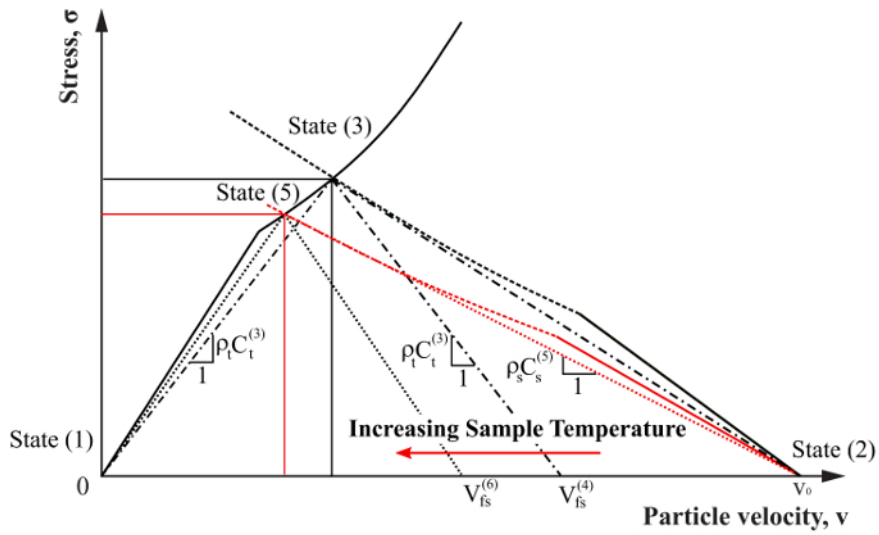

Figure 14: Stress versus particle velocity diagram for a reverse configuration normal plate impact experiment. This figure shows the stress versus particle velocity diagram for an elevated temperature reverse geometry normal plate impact experiment. The curve centered at origin details the locus of all stress states achievable for the isotropic target plate, whereas the curve originating at V_0 details the locus of all states for the sample material at room temperature, moreover, the red curve intersecting V_o is meant to show the possible effect of increasing temperatures. Upon impact against a room temperature sample, the target plate moves from an un-loaded state (1) to a loaded state (3), whereas, if impact is made against a pre-heated sample, the target will move from state (1) to state (5), consequently, shifting the free surface particle velocity states from (4) to (6). Please click here to view a larger version of this figure.

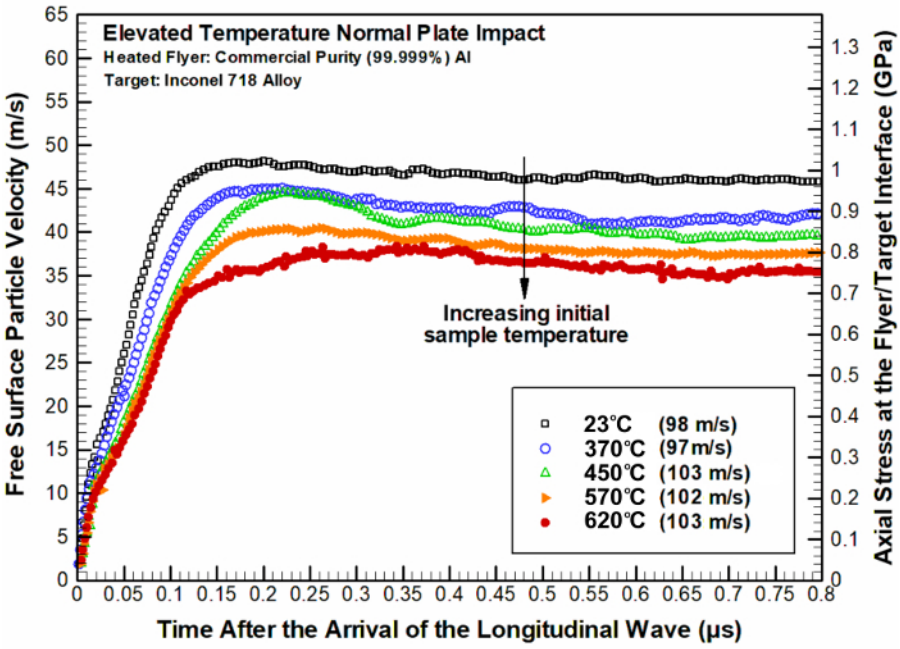

Figure 15: Normal free surface velocity record for the current experimental configuration. This figure shows the free surface particle velocity trace obtained from the normal motion diagnostics. This trace initially manifests a relatively sharp rise in velocity related to the dynamics of the impact, followed by a plateau resulting from an impedance match between the flyer and target plates which is sustained through the duration of the experiment. The initial velocity rise relates directly to the stress in the Al sample at the flyer/target interface as the shock evolves, whereas the velocity at the shock plateau is related to the impedance match between the target and flyer plates. Overall, the plot shows decreasing particle velocities throughout, with increasing temperatures, and this suggests possible thermal softening of the sample material under the current loading conditions. Please click here to view a larger version of this figure.

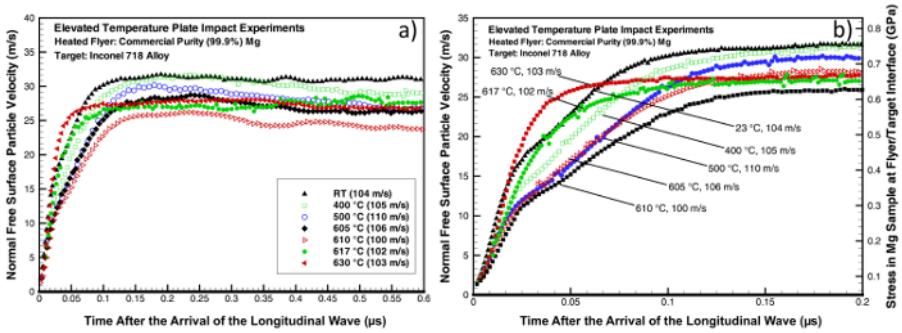

Figure 16. Normal free surface particle velocity trace obtained from experiments performed on commercial purity polycrystalline magnesium. (a) shows monotonically decreasing particle velocities at the shock plateau for temperatures ranging from room to 610 ˚C, however at higher temperatures (617, 630 ˚C), the trend is reversed. (b) shows that this increase in particle velocity is also apparent in the initial rise of the particle velocity trace. Please click here to view a larger version of this figure.

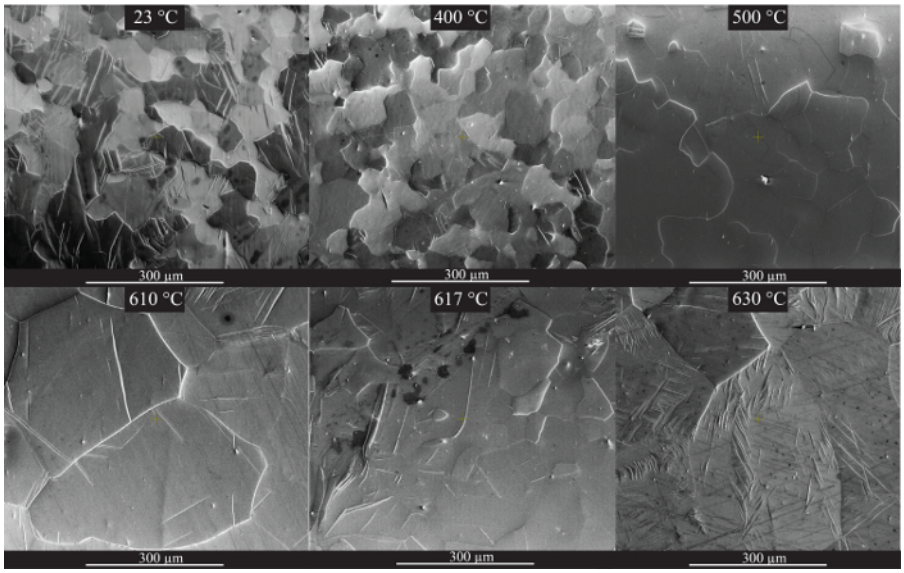

Figure 17. Microscale images of a cross-section of the post-impact test specimens. The images show two noticeable effects on the microstructure of the sample as a result of increasing temperature. First, the images show grain ripening with increasing sample temperature, but more interesting is the change in the twin band formations, which manifest as tabular features or lines with finite width that cut through grains. For temperatures ranging from 23 – 500 ˚C, a decrease in the twin band formation can be observed, however, as temperatures are increased beyond this point (i.e., 610, 617, 630 ˚C) a re-emergence of twin bands are clearly observed. Please click here to view a larger version of this figure.

Discussion

The method and protocol stated above detailed the procedure for properly performing a reverse geometry normal plate impact experiment at elevated temperatures. In this approach, we make custom modifications to the gun barrel at the high pressure (breech) end of the existing gas gun at Case Western Reserve University, to house a resistive heater coil with axial and rotational degrees of freedom. The resistive heater coil system enables thin aluminum specimens, held at the front-end of a heater resistant sabot, to be heated to near melting temperatures (in excess of 640 °C), prior to firing. Using the heater housing adaptation coupled with a heat resistant sabot, elevated temperature plate impact experiments were performed without the need for special experimental considerations, which are typical when utilizing the conventional approach, such as, the need for remote tilt adjustment with real-time feedback for maintaining parallelism of the target and flyer plates during the heating process. Overall, the new approach significantly reduces the number of steps in the protocol section, when compared to the conventional approach.

In the experimental protocol section, we detail the steps required for: 1) sample and target material preparation, where the flyer and target plates are carefully machined, lapped, and polished, to within the parallelism and flatness tolerances necessary for the generation of plane waves with a front sufficiently parallel to the impact surface; 2) assembly of custom heat-resistant sabot capable of securing a heated sample plate, while mitigating heat flow into the sabot body, and to the gun barrel. Additionally, the sabot houses a key, which mates to the existing key-way in the gun barrel to prevent rotation of the entire sabot assembly during its travel down the length of the gun-barrel. Lastly, in steps 3-5 we detail the protocol for alignment of the sample and target plates prior to conducting the experiments, heating the flyer plate (sample) and the execution of the experiments. In the subsequent section, we showed how the accuracy of the protocol could be verified from the raw data provided in **Figure 1**. Finally, we present results from successful elevated temperature normal plate impact experiments, which enable the measurements of stress/

particle velocity states at the sample/target interface, as well as, the temperature dependent longitudinal acoustic impedance of the sample material.

In the near future, with appropriate adjustments to the sabot design, this method is expected to enable even higher temperature plate impact experiments, which will enable its use in probing dynamic material behavior of higher melting point materials at near melting temperatures. Given the versatility of this approach, several different experimental configurations will be used to study dynamic material behavior across-the-board. For example, elevated temperature reverse geometry plate impact experiments can be suitably designed to make measurements of shock wave speeds in metals at increasing temperatures, while pressure-shear plate impact experiments can be performed to evaluate dynamic inelasticity at large strains and ultra-high shearing rates.

Disclosures

The authors have nothing to disclose.

Acknowledgements

The authors would like to acknowledge financial support of the U.S. Department of Energy through the Stewardship Science Academic Alliance DOE/NNSA (DE-NA0001989 and DE-NA0002919) in conducting this research. Finally, the authors would like to thank Los Alamos National Lab for their collaboration in support of undergoing efforts in the current and future investigations.

References

1. Davies, R. M. A critical study of the Hopkinson pressure bar. *Philosophical Transactions of the Royal Society of London. Series A, Mathematical and Physical Sciences.* **240**, 375-457 (1948).
2. Kolsky, H. An investigation of the mechanical properties of materials at very high rates of loading. *Proceedings of the Physical Society. Section B.* **62**, 676 (1949).
3. Gilat, A., & Cheng, C.-S. Torsional split Hopkinson bar tests at strain rates above 104s− 1. *Experimental Mechanics.* **40**, 54-59 (2000).
4. Harding, J., Wood, E., & Campbell, J. Tensile testing of materials at impact rates of strain. *Journal of Mechanical Engineering Science.* **2**, 88-96 (1960).
5. Clifton, R. J., & Klopp, R. W. Pressure-shear plate impact testing. *Metals handbook.* **8**, 230-239 (1985).
6. Zuanetti, B., Wang, T., & Prakash, V. Mechanical Response of 99.999% Purity Aluminum Under Dynamic Uniaxial Strain and Near Melting Temperatures. *International Journal of Impact Engineering.* **113**, 180-190 (2017).
7. Wang, T., Zuanetti, B., & Prakash, V. Shock Response of Commercial Purity Polycrystalline Magnesium Under Uniaxial Strain at Elevated Temperatures. *Journal of Dynamic Behavior of Materials.* **3**, 497-509 (2017).
8. Dike, S., Wang, T., Zuanetti, B., & Prakash, V. Dynamic Uniaxial Compression of HSLA-65 Steel at Elevated Temperatures. *Journal of Dynamic Behavior of Materials.* **3**, 510-525 (2017).
9. Okada, M., Liou, N.-S., Prakash, V., & Miyoshi, K. Tribology of high speed metal-on-metal sliding at near-melt and fully-melt interfacial temperatures. *Wear.* **249**, 672-686 (2001).
10. Prakash, V., & Clifton, R. J. *Fracture Mechanics: Twenty Second Symposium (vol. 1)*. Astm Special Technical Publication (1992).
11. Prakash, V., & Mehta, N. Uniaxial Compression and Combined Compression-and-Shear Response of Amorphous Polycarbonate at High Loading Rates. *Polymer Engineering and Science.* **52**, 1217-1231 (2012).
12. Lee, Y., & Prakash, V. Dynamic fracture toughness versus crack-tip speed relationship at lower than room temperature for high strength 4340VAR structural steels. *Journal of the Mechanics and Physics of Solids.* **46**, 1943-1967 (1998).
13. Lee, Y., & Prakash, V. Dynamic brittle fracture of high strength structural steels under conditions of plane strain. *International Journal of Solids and Structures.* **36**, 3293-3337 (1999).
14. Yuan, F., Prakash, V., & Lewandowski, J. J. Shear yield and flow behavior of a Zirconium-based bulk metallic glass. *Mechanics of Materials.* **42**, 248-255 (2010).
15. Shazly, M., Prakash, V., & Draper, S. Mechanical behavior of Gamma-Met PX under uniaxial loading at elevated temperatures and high strain rates. *International Journal of Solids and Structures.* **41**, 6485-6503 (2004).
16. Klopp, R., Clifton, R., & Shawki, T. Pressure-shear impact and the dynamic viscoplastic response of metals. *Mechanics of Materials.* **4**, 375-385 (1985).
17. Arvidsson, T. E., Gupta, Y., & Duvall, G. E. Precursor decay in 1060 aluminum. *Journal of Applied Physics.* **46**, 4474-4478 (1975).
18. Gilat, A., & Clifton, R. Pressure-shear waves in 6061-T6 aluminum and alpha-titanium. *Journal of the Mechanics and Physics of Solids.* **33**, 263-284 (1985).
19. Barker, L., & Hollenbach, R. Shock wave study of the α#ε phase transition in iron. *Journal of Applied Physics.* **45**, 4872-4887 (1974).
20. Shazly, M., & Prakash, V. Shock response of a gamma titanium aluminide. *Journal of Applied Physics.* **104**, 083513 (2008).
21. Yuan, F., Prakash, V., & Lewandowski, J. J. Spall strength and Hugoniot elastic limit of a Zirconium-based bulk metallic glass under planar shock compression. *Journal of Materials Research.* **22**, 402-411 (2007).
22. Yuan, F. P., Prakash, V., & Lewandowski, J. J. Spall strength of a zirconium-based bulk metallic glass under shock-induced compress ion-and-shear loading. *Mechanics of Materials.* **41**, 886-897 (2009).
23. Prakash, V. A pressure-shear plate impact experiment for investigating transient friction. *Experimental Mechanics.* **35**, 329-336 (1995).
24. Kumar, P., & Clifton, R. Optical alignment of impact faces for plate impact experiments. *Journal of Applied Physics.* **48**, 1366-1367 (1977).
25. Prakash, V. Time-resolved friction with applications to high speed machining: experimental observations. *Tribology Transactions.* **41**, 189-198 (1998).
26. Frutschy, K., & Clifton, R. High-temperature pressure-shear plate impact experiments using pure tungsten carbide impactors. *Experimental mechanics.* **38**, 116-125 (1998).

27. Frutschy, K., & Clifton, R. High-temperature pressure-shear plate impact experiments on OFHC copper. *Journal of the Mechanics and Physics of Solids.* **46**, 1723-1744 (1998).
28. Zaretsky, E., & Kanel, G. I. Effect of temperature, strain, and strain rate on the flow stress of aluminum under shock-wave compression. *Journal of Applied Physics.* **112**, 073504 (2012).
29. Grunschel, S. E. *Pressure-shear plate impact experiments on high-purity aluminum at temperatures approaching melt.* Brown University, (2009).
30. Zuanetti, B., Wang, T., & Prakash, V. A Novel Approach for Plate Impact Experiments to Determine the Dynamic Behavior of Materials Under Extreme Conditions. *Journal of Dynamic Behavior of Materials.* **3**, 64-75 (2017).
31. Zuanetti, B., Wang, T., & Prakash, V. A compact fiber optics-based heterodyne combined normal and transverse displacement interferometer. *Review of Scientific Instruments.* **88**, 033108 (2017).
32. Zuanetti, B., Wang, T., & Prakash, V. Mechanical response of 99.999% purity aluminum under dynamic uniaxial strain and near melting temperatures. *International Journal of Impact Engineering.* **113**, 180-190 (2018).
33. Duffy, T. S., & Ahrens, T. J. Compressional sound velocity, equation of state, and constitutive response of shock-compressed magnesium oxide. *Journal of Geophysical Research: Solid Earth.* **100**, 529-542 (1995).
34. Tan, Y. *et al.* Hugoniot and sound velocity measurements of bismuth in the range of 11-70 GPa. *Journal of Applied Physics.* **113**, 093509 (2013).

